IEEE Access
Multidisciplinary | Rapid Review | Open Access Journal

Received 31 May 2024, accepted 13 June 2024, date of publication 21 June 2024, date of current version 28 June 2024.

Digital Object Identifier 10.1109/ACCESS.2024.3417488

RESEARCH ARTICLE

Automated 3D Tumor Segmentation From Breast DCE-MRI Using Energy-Tuned Minimax Optimization

PRIYADHARSHINI BABU, MYTHILI ASAITHAMBI, AND SUDHAKAR MOGAPPAIR SURIYAKUMAR
School of Electronics Engineering, Vellore Institute of Technology, Vellore, Tamil Nadu 632014, India
Corresponding author: Mythili Asaithambi (mythili.asaithambi@vit.ac.in)

ABSTRACT Breast cancer (BC) is a multifaceted genetic malignancy that accounts for the majority of cancer fatalities in women. Dynamic Contrast-Enhanced Magnetic Resonance Imaging (DCE-MRI) is predominant in evaluating perfusion, extravascular-extracellular volume fraction, and microvascular vessel wall permeability in breast cancer patients. Precise tumor segmentation using DCE-MRI is a key component of assessing diagnosis and treatment planning. However, the slice-wise analysis of DCE-MRI fails to preserve 3D surface continuity and is insufficient for evaluating the invasion depth of the tumor. Hence, this work proposes an analytical model labeled as Bezier-tuned Energy Functionals optimized via variational minimax for Volumetric Breast Tumor Segmentation (BEFVBTS). The formulated energy functionals consist of non-linear convex edge-sensitive data and regularization terms. Also, the variational minimax technique adopts gradient descent with an exact line search algorithm for obtaining a global minimax solution. The self-analysis of BEFVBTS on the Duke- Breast-Cancer-MRI dataset registered remarkable performance in segmenting tumors with different grades (Grade 1,2 & 3). Likewise, the relative analysis on QIN Breast DCE-MRI and TCGA-BRCA datasets revealed improvements of 8%, 22%, 8.7%, 4%, 0.120%, and 68.17% in Dice, Jaccard, Precision, Sensitivity, Specificity, and Hausdorff distance (HD) respectively over the recent competitors. At last, the complexity analysis of the model demonstrated simplicity and amicability for its extension to real-time clinical applications.

INDEX TERMS BEFVBTS, DCE-MRI, energy functionals, line search, variational minimax optimization.

I. INTRODUCTION

Despite drastic advancements in cancer studies, BC continues to be an extremely prevalent disease [1]. A study by the World Health Organization (WHO) has reported that 2.3 million women were diagnosed with BC in 2022, and the count is expected to increase by 3 million in 2040 [2]. Hence, their early detection would direct the patients to anti-cancer therapies that aid in recovery with long-term survival [3]. Few breast imaging modalities such as mammography [4], ultrasound [5], thermograms [6], [7], and MRI [8] are reliable for screening, diagnosis, preoperative evaluation, and follow-ups in BC patients [9]. Especially, DCE-MRI has gained interest owing to its high sensitivity in capturing morpho-functional features that project biological changes in breast tissues [10]. Also, DCE-MRI capitulates the tumor's neo-vasculature occurring before any volumetric changes in the tumor [11]. In general, slice-wise DCE-MRI tumor segmentation fails to retain 3D surface continuity and interslice correlation. Rather, volumetric segmentation captures the spatial information of the tumor across the axial, sagittal, and coronal axes by evaluating the tumor's invasion depth and its connection to the surrounding tissue. Further, manually annotating 3D images is time-consuming due to the large number of slices and complexity of tumor structure. In contrast, automatic segmentation is fast, time-saving, and

The associate editor coordinating the review of this manuscript and approving it for publication was Orazio Gambino.

accurate, thereby, reducing the load on clinicians. Hence, this work proposes an analytical model that is Bezier-tuned and optimized via variational minimax for volumetric tumor segmentation.

The chronological list of automated segmentation models available in the literature is presented to understand the novelty of the proposed work. The traditional segmentation models exploit pixel homogeneity and discontinuity based on morphological features [12] using thresholding [13], region growing [14], and watershed [15], [16] techniques. Although these models registered excellent segmentation results, their performance declined when dealing with heterogeneous tumors. Alternately, Active contours (AC) [17], and fuzzy C means (FCM) [18] have established superiority by overcoming artifacts and ambiguous edge concerns. For instance, the AC variant named spectral embedding-based active contours (SEAC) [19] captured the strong gradients across the regional boundaries offering larger intensity separations between tumor and non-tumor regions. SEAC accomplishes it by using the eigenvector-based voxel analysis for better lesion segmentation. However, the bias field correction applied to the image and non-optimized weight parameters dragged down the models' performance. Likewise, the soft computed FCMs ignored the spatial voxel relationship and were prone to noise. To overcome this, the spatial FCM was proposed [20] that regularizes the data terms by adding a penalty to a unique objective function. However, this process necessitates manual modification of FCM parameters and the predetermined ROI selection involves human intervention [21].

The advent of data-driven deep-learning techniques superseded these models and is widely utilized in tumor segmentation despite the demand for the enormous annotations needed for training. Such recent networks UNet3D, Vnet, UNETR, nnU-Net, U-Node3D, and Att-U-Node3D have gained research interest in 3D (volumetric) segmentation [22]. However, their extension to volumetric analysis still requires deeper exploration. Herein few such DL contributions are brought forth to understand their impact on volumetric analysis and their related issues. Just recently, the 3D U-Net transformer (UNETR) [23] was trained with weak annotations for isolating the whole breast from the ROI using bounding boxes. The pre-annotated ground truths showed satisfactory results while the model relied extremely on manual annotations. Similarly, the 3D patch-based modified U-Net [24] merged residual blocks with ROI-restricted balanced patches to overcome the class imbalance and organ differentiation issues that had surpassed the state-of-the-art segmentation methods regardless of dataset complexities. Alternatively, the attention-guided ODE network (Att-U-Node3D) [22] used the convolutional block attention module (CBAM) for capturing the spatial and channel information, and encoder-decoder compartments for feature extraction and recovery, and a neural ODE for feature modeling. Likewise, the three 3D U-Net [25] employed subtraction and post-contrast images or a combination of them at the feature level to obtain complementary information and utilized a visual ensemble selection process to choose the most optimal segmentation. The multi-label attention-guided model joint phase net (AJPN) [26] model fused diverse comprehensive features with time-signal intensity maps for ROI localization. Instead, the mask-guided hierarchical learning (MHL) framework [27] generated a 3D breast mask ROI for precise and accurate tumor segmentation using a 2-stage fully convolutional network (FCN). Another convolution network [28] employed multi-scale context (M2D3D-MC) to achieve greater transferability and low inference time in 2D. Also, its prominence in learning contextual information in 3D tumor segmentation even with a bounded number of axial slices was highly beneficial.

Although the aforementioned DL methods achieved superiority in segmenting breast tumors, their computations demand sophisticated and specialized hardware resources for model training [29] and eventually tend to overfit for untrained data. Additionally, the fairness of these models is down-laid owing to the over-parametrization in determining the local minimum and remains NP-hard due to the ubiquitous existence of saddle points. Also, most of the DL involves non-convex optimization with multiple local minima which is still challenging for obtaining optimal solutions [30]. Rather, analytical models are interpretive, rapid, and they exhibit parameter dependencies explicitly.

To address the wider range of issues encountered by traditional and recent peers, this work introduces variational minimax optimization with novel energy functionals consisting of non-linear convex combinations of data and regularization terms. The data term stimulates the generated heterogeneous volume to interact with the image volume at a higher gradient point while the regularization smoothens the edge points. The variational minimax optimization is utilized to minimize or maximize the weight parameter to obtain the optimal heterogeneous volume. Further, the introduced model aims to reduce the number of optimization parameters while assuring generalization, robustness, sparsity, monotonicity, and decomposability. The manuscript is systematized as follows: Section I introduces the background of the formulated BEFVBTS framework and articulates its significance by chronologically outlining the pros and cons of the related peers. Section II formulates the BEFVBTS's methodology, while Section III rigorously assesses its performance. The amicability of the BEFVBTS's extension to a real-time scenario is studied in terms of its realization complexities in Section IV. Finally, the model is briefly summarized with an outline of the future research direction.

II. METHODOLOGY

DCE-MRIs are packed with diverse intensity variations constituting the breast and chest regions. Hence, it is crucial to effectively capture these intensity variations in DCE-MRI for precise ROI localization. To perform this, three novel edge-sensitive energy functionals are introduced to project the homogeneous and heterogeneous regions in the DCE-MRI. The proposed model also adopts a highly

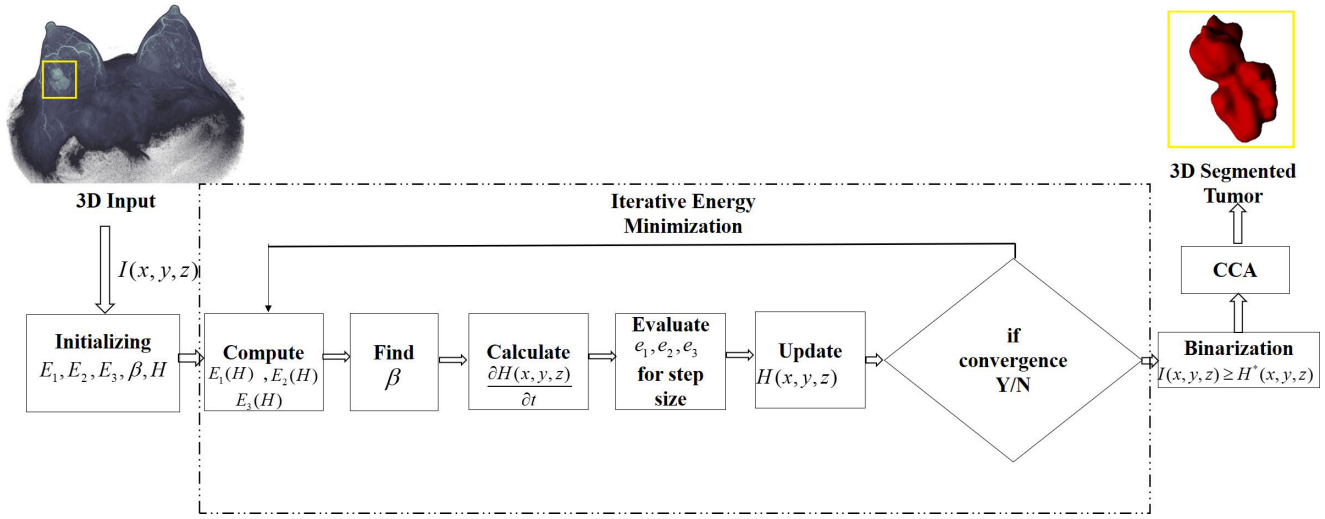

FIGURE 1. Flow diagram of BEFVBTS.

localized and adaptive data fitting technique named as parametric Quadratic Bezier Curve due to its application in medical image segmentation [31]. The Bezier Curve hyperparameters further weight these functionals to yield the convex optimization equation [32].

A. FRAMEWORK OVERVIEW

The process diagram of the BEFVBTS framework is shown in Fig.1. The flow commences with loading the input volume $I(x, y, z)$, followed by initializing the energy functionals E_1,E_2,E_3 and hyper-parameter β. The iterative energy minimization process involves computing $E_1(H)$, $E_2(H)$ and $E_3(H)$ that consists of edge-sensitive terms $H(x, y, z)$ made to interacts with the input volume $I(x, y, z)$ at high gradient places. The calculation of the hyper-parameter (β), the optimum heterogeneous volume $H(x, y, z)$, and the optimal step size take place at each iteration. Finally, the heterogeneous volume is updated by the updation rule. Upon convergence, binarization followed by CCA (Connected Component analysis) is performed, otherwise, the process continues until convergence. The convex optimization equation encompassing three energy functionals is given in Eq.(1),

$$E(H;\beta) = (1-\beta)^2 E_1(H) + 2\beta(1-\beta)E_2(H) + \beta^2 E_3(H) \tag{1}$$

$E_1(H)$, $E_2(H)$ are the data terms, and $E_3(H)$ is the regularization term. The role of multivariate Hessian matrix ($H(x, y, z)$) is to capture the surface variations across each dimension and is essential for approximating quadratic functions. The voxels are normalized for analyzing higher dimensional images with large intensity variations. Also, the overall energy of the volume is assumed to be '1' which comprises both tumor and non-tumor voxels. The normalized Hessian capturing the intensity variation is given by,

$$H(x, y, z) = \frac{\left|\nabla^2 I(x, y, z)\right|}{\max(\left|\nabla^2 I(x, y, z)\right|)} \tag{2}$$

$H(x, y, z)$ in Eq. (2) refine the edge information to achieve precise and adaptive segmentation. Hessian utilization in BEFVBTS assures localization of High-Frequency Features (HFF) and refinement of innate details concerned with object boundaries. The first energy functional $E_1(H)$ is the energy from the deviation between two volumes $H(x, y, z)$ and $I(x, y, z)$.

$$E_1(H) = \frac{1}{3}\iiint [H(x, y, z) - I(x, y, z)]^2 \, dx\, dy\, dz \tag{3}$$

The difference between the two volumes in Eq.(3) retains the homogeneous regions that almost pack the maximum energy and neglect the heterogeneous regions. In contrast, the second energy-functional $E_2(H)$ is the energy that retains the heterogeneous regions by multiplying $H(x, y, z)$ and $I(x, y, z)$.

$$E_2(H) = \frac{1}{3}\iiint [H(x, y, z) * I(x, y, z)]^2 \, dx\, dy\, dz \tag{4}$$

Finally, $E_3(H)$ in Eq. (5) is the energy of gradient of the heterogeneous volume $H(x, y, z)$.

$$E_3(H) = \frac{1}{3}\iiint |\nabla H(x, y, z)|^2 \, dx\, dy\, dz \tag{5}$$

To achieve optimized segmentation, the cost function $E(H; \beta)$ is minimized. Accordingly, minimizing the data terms results in the interaction of heterogeneous volume and image volume at high gradient points, whereas minimizing the regularization term smoothens the heterogeneous volume by degrading high-frequency features. The optimum heterogeneous volume necessitates a minimax solution for the function $\max_H \min_\beta E(H; \beta)$. This solution ensures that the

weight parameter β conciliates inequalities between data and the regularization term, thereby circumventing spurious and under-segmentation. Owing to the concave-convex nature of $E(H;\beta)$ the order interchange from min to max or max to min is possible since the duality gap between the β and H is zero [33] shown in Eq.(6).

$$H^* = \arg\max_H \min_\beta E(H;\beta) = \arg\max_\beta \min_H E(H;\beta) \quad (6)$$

The following sections detail the steps in finding the optimum weighted parameter, heterogeneous volume, and step size.

1) CALCULATION OF β

To obtain β^*, calculate $\frac{\partial E(H;\beta)}{\partial \beta} = 0$ which yields a conventional solution that stabilizes the data term present in the energy functionals.

$$\beta^* = \frac{E_1 - E_2}{E_1 - 2E_2 + E_3} \quad (7)$$

2) CALCULATION OF OPTIMAL H

The differential heterogeneous volume presented in Eq. (8) is the Euler-Lagrange differential equation [34] that calculates the variation of E with respect to H in all three directions. For a fixed value of β referred to as β^*, the equation E_f is given in Eq. (9).

$$\frac{\partial H(x,y,z)}{\partial t} = -E_f \quad (8)$$

$$E_f = \frac{\partial E}{\partial H} - \frac{\partial E}{\partial H_x} - \frac{\partial E}{\partial H_y} - \frac{\partial E}{\partial H_z} \quad (9)$$

where $H_x = \frac{\partial H}{\partial x}$, $H_y = \frac{\partial H}{\partial y}$, and $H_z = \frac{\partial H}{\partial z}$. After substituting the derived parameters in Eqt. (9), the overall Euler-Lagrange equation is given in Eqt. (10).

$$\begin{aligned} E_f = {} & \frac{2}{3}(1-\beta^*)^2(H-I) \\ & + \frac{4}{3}(\beta^* - \beta^{*^2})(I.H) \\ & - \frac{1}{3}\beta^{*^2}(H_{xx} + H_{yy} + H_{zz}) \end{aligned} \quad (10)$$

where $H_{xx} = \frac{\partial^2 H}{\partial x^2}$, $H_{yy} = \frac{\partial^2 H}{\partial y^2}$, and $H_{zz} = \frac{\partial^2 H}{\partial z^2}$. Similarly the change in heterogeneous volume in Eqt. (8) is given by,

$$\begin{aligned} \frac{\partial H(x,y,z)}{\partial t} = {} & -\frac{2}{3}(1-\beta^*)^2(H-I) \\ & - \frac{4}{3}(\beta^* - \beta^{*^2})(I.H) + \frac{1}{3}\beta^{*^2}(\nabla^2 H) \end{aligned} \quad (11)$$

B. NUMERICAL IMPLEMENTATION

The discrete form of Eq.(11) is given in Eq.(12).

$$\begin{aligned} H_{lmn}^{t+1} = {} & H_{lmn}^t + \tau[-\frac{2}{3}(1-\beta^*)^2(H_{lmn}^t - I_{lmn}) \\ & - \frac{4}{3}(\beta^* - \beta^{*^2})(I_{lmn}.H_{lmn}^t) + \frac{1}{3}\beta^{*^2}(\nabla^2 H_{lmn}^t)] \end{aligned} \quad (12)$$

where τ is the step size that changes iteratively and t is the iteration number. This explicit method for calculating the solution is simple to implement and also requires less computation.

1) CALCULATION OF STEP SIZE (τ)

The step size τ determines the accuracy of the solution obtained and is crucial in optimization. To determine the optimum step size, the segmentation model utilizes the exact line search algorithm [35], [36] via the steepest descent. For instance, $E(H^{(k)} + \tau^{(k)}\delta H^{(k)})$ be the cost function to be minimized at k^{th} iteration, the total energy function is distributed as in Eq. (13). Details are in Appendix B.

$$E(H^{(k)} + \tau^{(k)}\delta H^{(k)}) = E_1 + E_2 + E_3 \quad (13)$$

where

$$E_1 = \frac{1}{3}(1-\beta^{(k)})^2 \sum (H^{(k)} + \tau^{(k)}\delta H^{(k)} - I)^2 \quad (14)$$

$$E_2 = \frac{2}{3}\beta^{(k)}(1-\beta^{(k)}) \sum (I * (H^{(k)} + \tau^{(k)}\delta H^{(k)}))^2 \quad (15)$$

$$E_3 = \frac{1}{3}(\beta^{(k)})^2 \sum \left\| \nabla(H^{(k)} + \tau^{(k)}\delta H^{(k)}) \right\|^2 \quad (16)$$

Eq. (13) is rearranged as shown in Eq. (14),

$$E(H^{(k)} + \tau^{(k)}\delta H^{(k)}) = e_1 + \tau^{(k)}e_2 + (\tau^{(k)})^2 e_3 \quad (17)$$

where

$$\begin{aligned} e_1 = {} & \frac{1}{3}(1-\beta^{(k)})^2 \sum (H^{(k)} - I)^2 \\ & + \frac{2}{3}\beta^{(k)}(1-\beta^{(k)}) \sum (I * H^{(k)})^2 \\ & + \frac{1}{3}(\beta^{(k)})^2 \sum \left\| \nabla H^{(k)} \right\|^2 \end{aligned} \quad (18)$$

$$\begin{aligned} e_2 = {} & \frac{2}{3}(1-\beta^{(k)})^2 \sum (H^{(k)} - I)\delta H^{(k)} \\ & + \frac{4}{3}\beta^{(k)}(1-\beta^{(k)}) \sum (I^2 * H^{(k)}\delta H^{(k)}) \\ & + \frac{2}{3}(\beta^{(k)})^2 \sum \nabla H^{(k)}.\nabla(\delta H^{(k)}) \end{aligned} \quad (19)$$

$$\begin{aligned} e_3 = {} & \frac{1}{3}(1-\beta^{(k)})^2 \sum (\delta H^{(k)})^2 \\ & + \frac{2}{3}\beta^{(k)}(1-\beta^{(k)}) \sum (I * \delta H^{(k)})^2 \\ & + \frac{1}{3}(\beta^{(k)})^2 \sum \left\| \nabla \delta H^{(k)} \right\|^2 \end{aligned} \quad (20)$$

The optimal $\tau^{(k)}$ is measured by differentiating Eq. (13) to $\tau^{(k)}$ and equating to zero.

$$\tau^{(k)} = -\frac{e_2}{2e_3} \quad (21)$$

Finally, iterative steps in the BEFVBTS framework are,
Step 1: Initialize H
Step 2: While (for convergence not reached)
a. Compute $E_1(H)$,$E_2(H)$ and $E_3(H)$
b. Compute β
c. Determine the search direction $\delta H^{(k)}$
d. Compute the optimum value of τ
e. Arrange $H^{(k+1)} = H^{(k)} + \tau^{(k)}\delta H^{(k)}$
End while

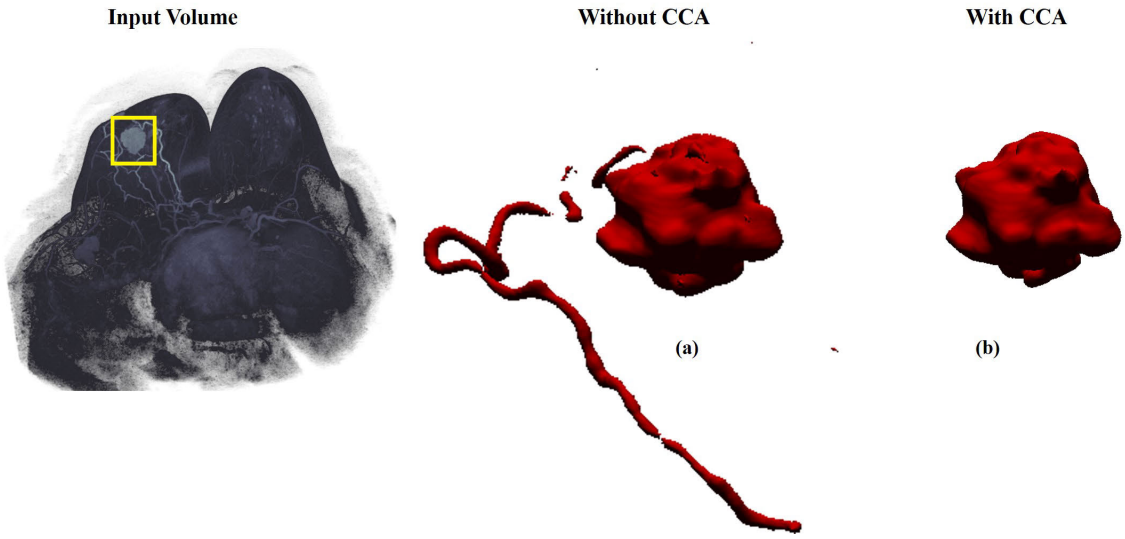

FIGURE 2. The role of CCA in the BEFVBTS framework.

C. BINARIZATION USING THE UPDATED HESSIAN

The updated heterogeneous volume $H^*(x, y, z)$ is compared with the input $I(x, y, z)$ using Eq. (22) to yield the binary equivalent [37].

$$I_{\text{Binarized}} = \begin{cases} 1 & \text{for } I(x, y, z) \geq H^*(x, y, z) \\ 0 & \text{elsewhere} \end{cases} \tag{22}$$

D. RESIDUAL REMOVAL

Although BEFVBTS performs satisfactory segmentation, the binarization process also picks the voxels that are residual besides the VOI. Therefore, there is a need to isolate these residual voxels based on their connectivity strength for acute localization. Further, the voxels corresponding to the tumor voxels in DCE-MRIs are packed with high connectivity,therefore it is easy to remove binarized residual non-tumor voxels based on their connectivity strength. Accordingly, Connected Component Analysis (CCA) [38], [39] is engaged as a post-binarization process to refine the ROI with voxels having higher affinity. CCA incorporation is verified qualitatively in Fig. 2. Fig. 2 demonstrates the importance of CCA in the framework. Fig. 2 (a) is the original input volume and Fig. 2 (b) shows the segmentation process without CCA where the presence of fibro-glandular tissues around the tumor is not completely evaded. However, CCA's significance is visualized in Fig. 2 (c) wherein the residual non-tumor voxels are evaded from the VOI.

III. PERFORMANCE ANALYSIS

The proposed model's efficiency is analyzed by conducting ROC investigations on popular benchmark datasets discussed below.

A. DATASET DESCRIPTION

The following datasets are involved in the performance analysis of BEFVBTS.

1) DUKE- BREAST-CANCER-MRI

The DCE-MRIs of 922 individuals with BC were obtained from The Cancer Imaging Archive (TCIA), which makes up this publicly available dataset [40]. These axial DCE-MRIs were obtained utilizing 1.5T or 3T scanners (GE Healthcare and Siemens) in the prone position. The MRI sequences, which include a fat-saturated gradient echo T1-weighted pre-contrast sequence, four post-contrast T1-weighted sequences, and a non-fat-saturated sequence, are acquired using the following parameters: 3.54-7.39 ms for the repetition time (TR), 1.25-2.76 ms for the echo time (TE), 320 × 320 for the acquisition matrix, 448 × 448 for the array size, 250-480 mm for the FOV (Field of View), and 7-12 degrees for the flip angle.

2) QIN BREAST DCE-MRI

This dataset includes DCE-MRIs obtained from TCIA on 10 patients at 20-time points [40]. These axial DCE-MRIs were obtained using the Siemens 3T TIM Trio system's TWIST (Time-resolved Angiography With Stochastic Trajectories) mode. The scanned 3D data is made up of 32-34 image volume sets with 112-120 slices acquired with the following settings: 1.4 mm slice thickness, 2.9 ms for repetition time, 6.2 ms for echo time, 320 × 320 acquisition matrix, 2 for acceleration, 30-34 cm field of view, and a 10-degree flip angle.

3) TCGA-BRCA

This freely available dataset includes DCE-MRIs obtained from 46 breast cancer patients from TCIA [40]. All of the examples involve biopsies that reveal at least one primary lesion. DCE-MRIs from the University of Pittsburgh Medical Centre (1999-2004) were recorded before treatment utilizing a 1.5T GE whole-body MRI scanner (GE Medical Systems, Milwaukee, Wisconsin, USA). The dataset contains one pre-contrast and 4-6 post-contrast DCE-MRI volumes

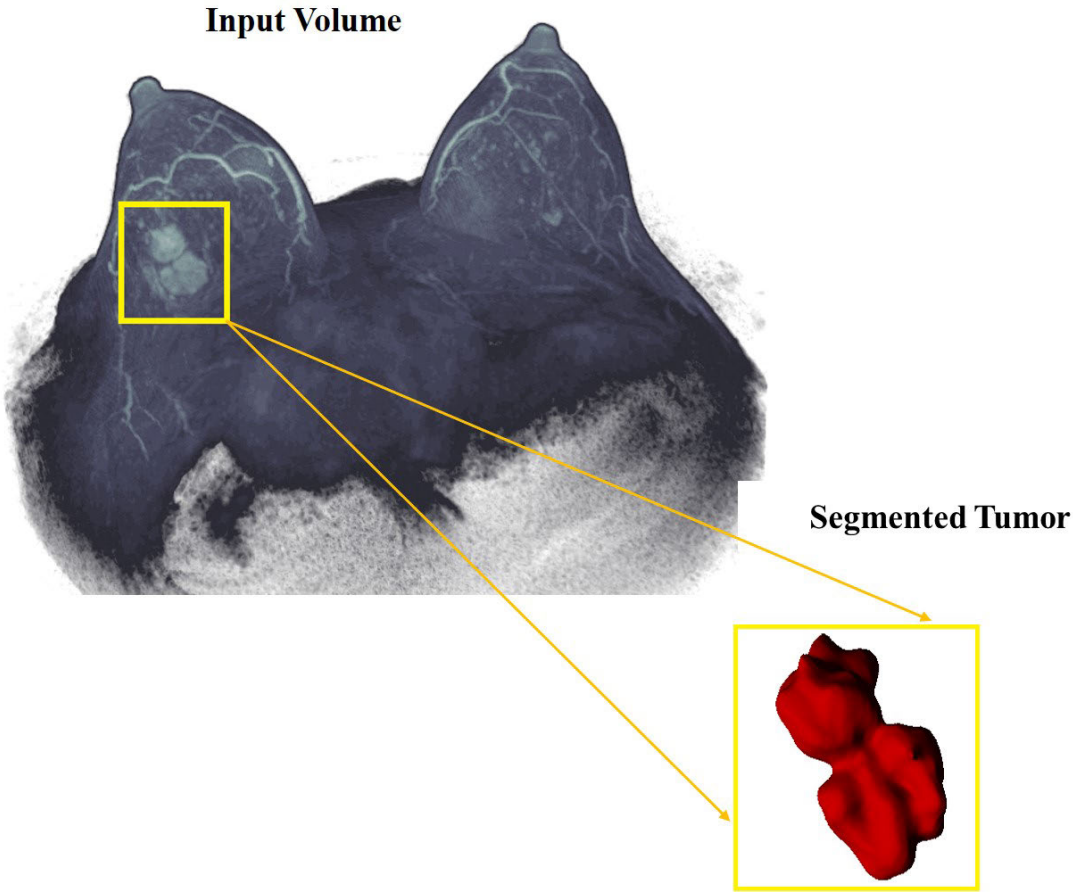

FIGURE 3. Sample DCE-MRI showing multifaceted tumor segmented using BEFVBTS framework.

obtained using a T1-weighted 3D spoiled gradient echo sequence. The acquired slices are spaced at 2-3 mm with a resolution of 0.53-0.86 mm and have a dimension of 512 × 512 with the slices piled to 85112.

B. ROC METRICS

The scheme adopts conventional Receiver operating characteristic (ROC) metrics engaged by traditional and trending schemes for both self and relative analysis. The choice of ROC parameters for segmentation analysis is owed to their ability to quantify how well the model has segmented the tumor same as the ground truth. Hence, higher ROC values signify the closeness of the segmented tumor with the ground truth volume. These parameters are evaluated using True Negative (TN), False Negative (FN), True Positive (TP), and False Positive (FP) factors. Let X segmented output and Y be the Ground Truth volume, the terms TP, TN, FP, and FN are designated as $X \cap Y$, $\overline{X \cap Y}$, $X \cap \overline{Y}$, and $\overline{X} \cap Y$ respectively. Based on these definitions the various ROC metrics namely Dice, Jaccard index, Precision, Sensitivity, Specificity, and HD95 (Hausdorff Distance) [22] modeled in Equations (23) - (28) are evaluated to validate the model's performance.

$$Dice = \frac{2TP}{2TP + FP + FN} \tag{23}$$

$$Jaccard\ \text{index} = \frac{TP}{TP + FP + FN} \tag{24}$$

$$\Pr ecision = \frac{TP}{TP + FP} \tag{25}$$

$$Sensitivity = \frac{TP}{TP + FN} \tag{26}$$

$$Specificity = \frac{TN}{TN + FP} \tag{27}$$

For segmented and ground truth volume, the Hausdorff distance is described in Eq. (28).

$$H(X, Y) = \max(h(X, Y), h(Y, X)) \tag{28}$$

$h(X, Y) = \max_{x \in X} \min_{y \in Y} \|x - y\|$ where x and y are the edge points belonging to X and Y respectively and $\|.\|$ is Euclidean norm. Generally, the Hausdorff distance between the segmented output and ground truth volume is evaluated as the minimum value since large distances depict more dissimilarities.

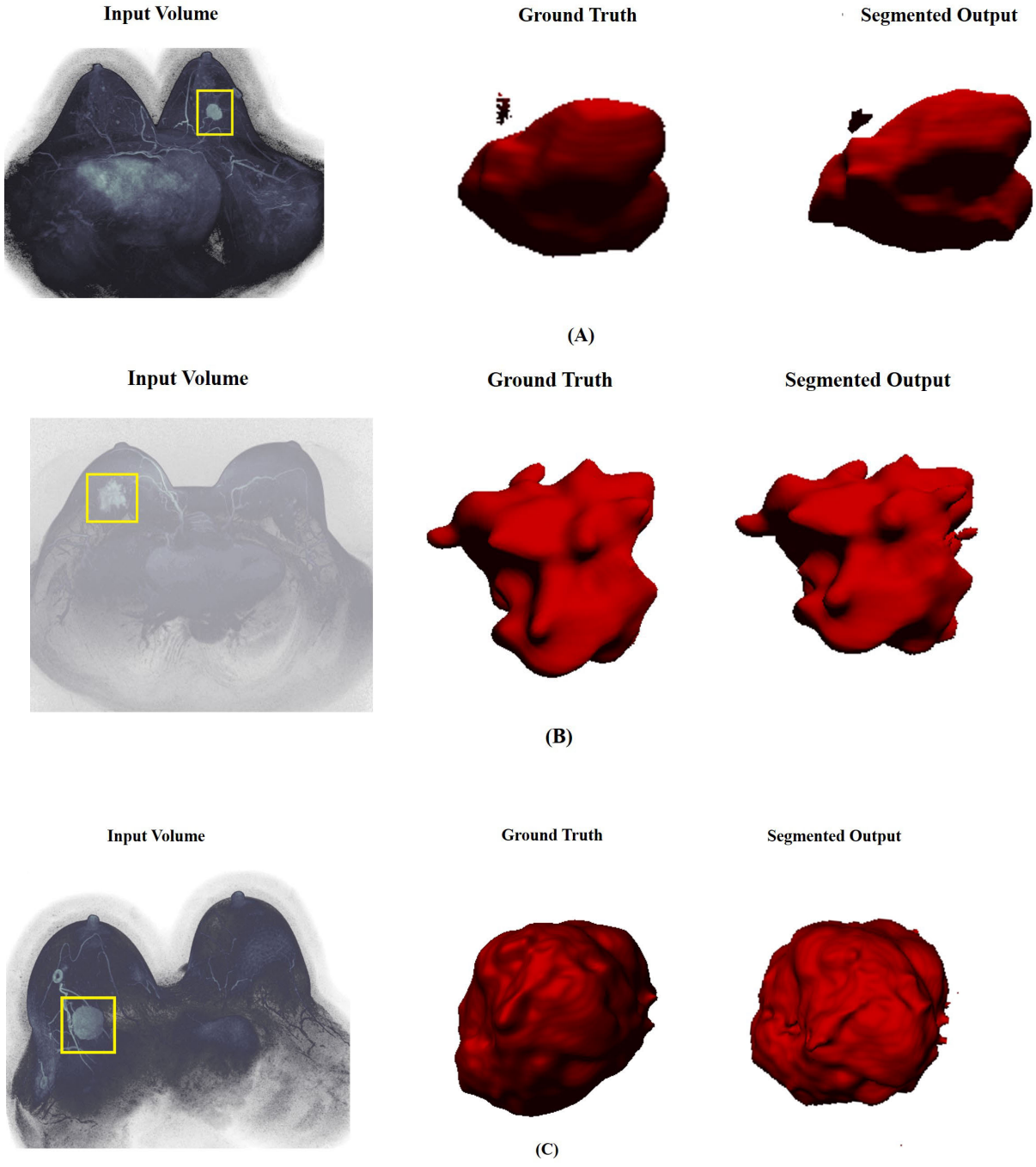

FIGURE 4. 3D Visuals of DCE-MRI segmentation on all three Grades using the BEFVBTS framework. (VI) Grade 1 segmentation with Dice = 0.85 and HD95 = 3.38. (VI) Grade 2 segmentation with Dice = 0.90 and HD95 = 3.02. (C) Grade 3 segmentation with Dice = 0.81 and HD95 = 5.20. Column 1 (Input Volume), Column 2 (Ground Truth), Column 3(Segmented Output).

C. IMPLEMENTATION AND RELATIVE ANALYSIS

The proposed framework is realized in MATLAB (R2021a) executed by 2.40 GHz Intel(R) Core(TM) running on a 64-bit Windows 11 operating system. To understand the scalability, reliability, and efficacy a detailed self-analysis was done on the DCE-MRIs from the Duke- Breast-Cancer-MRI with patients segregated based on Grades (1,2, and 3) and tumor location (unilateral). Further, the DCE-MRI volumes are converted into NIFTI format and cropped to 64 × 64 × 64. The 3D output volumes are viewed using Matlab(R2021a). The QIN Breast DCE-MRI dataset has been tested on the popular DL segmentation models such as U-Node3D, Att- U-Node3D, UNETR, UNet3D, nnU-Net, and VNet [22] where the same has been utilized to generalize the proposed model.

TABLE 1. Quantitative Analysis of BEFVBTS on Duke- Breast-Cancer-MRI.

Grade	Dice (↑)	Jaccard (↑)	Precision (↑)	Sensitivity (↑)	Specificity (↑)	HD (↓)
Grade 1	80.69	73.43	96.86	74.62	99.89	4.52
Grade 2	82.29	74.43	97.34	75.39	99.92	4.39
Grade 3	79.19	71.14	92.98	72.07	99.45	5.23

TABLE 2. Quantitative analysis of BEFVBTS on QIN Breast DCE-MRI.

Method	Dice (↑)	Jaccard (↑)	Precision (↑)	Sensitivity (↑)	Specificity (↑)	HD (↓)
UNet3D	64.84	52.10	73.07	74.64	99.13	18.57
VNet	65.49	51.45	72.34	72.76	99.46	16.67
UNETR	63.51	48.66	68.10	74.71	99.30	26.48
nnU-Net w/o *PP	61.07	49.01	67.13	74.43	99.42	19.04
nnU-Net w/*PP	63.35	51.47	69.72	74.43	99.55	12.88
U-Node3D	63.03	48.71	68.71	75.27	99.55	11.86
Att-U-Node3D	69.70	55.57	76.22	75.39	99.68	14.53
BEFVBTS	**75.54**	**69.64**	**83.16**	**78.57**	**99.80**	**5.83**

*PP-Post Processing

TABLE 3. Quantitative analysis of BEFVBTS on TCGA-BRCA.

Method	Dice (↑)	Jaccard (↑)	Precision (↑)	Sensitivity (↑)	Specificity (↑)	HD (↓)
primary lesions alone [24]	80.20	-	-	-	-	-
secondary lesions alone [24]	68.00	-	-	-	-	-
BEFVBTS	**79.90**	**69.00**	**86.20**	**78.36**	**99.94**	**4.76**

These models were trained by augmenting the dataset with images flipped horizontally, vertically, and randomly upon corrupting with Gaussian noise.

IV. RESULTS AND DISCUSSION

A. SEGMENTATION ON DUKE- BREAST-CANCER-MRI

This dataset is utilized in testing the BEFVBTS's qualitative and quantitative nature under different contexts. The required ground truth for the analysis was outlined by the expert from the Department of Radiology, Cincinnati Children's Hospital Medical Center, Cincinnati, United States. At the onset, the qualitative analysis of BEFVBTS is visualized in Fig.3 wherein its VOI localization and refining ability was well acknowledged. Accordingly, a sample unilateral DCE-MRI breast cancer patient with heterogeneous tumor shape and size is chosen and their segmentation result is depicted in Fig. 3.

The efficiency in segmenting tumors is due to the nonlinear function consisting of the edge-sensitive components to segregate tumor and non-tumor volume. Further, a grade-wise analysis is performed to reveal the consistency of the proposed framework. Accordingly, a total of 60 breast cancer patients with single and multifocal tumors were chosen and their ground truth are delineated by the expert. Generally, the tumors are categorized as high (Grade 3) due to their large size and shape with high intensity and low (Grade 1 & 2) that are smaller in mass with moderate intensity. The volume rendering of this qualitative analysis including all three grades segmented using BEFVBTS is shown in Fig. 4 (A, B, C).

In Fig. 4, the 1st column is the input DCE-MRI volume, and the 2nd, and 3rd columns represent ground truth and segmented output respectively. Upon observing Fig.4, it is evidenced that the segmentation model is highly adaptable and consistent in segmenting small and asymmetrical volumes. Further, to visualize the retainment of inter-slice correlation in segmentation the 2D visuals are shown in Fig.5.

For 2D visuals, a sample of two cases (1 and 2) where case 1 has a larger size and more irregularly shaped tumor and case 2 has a small mass with an oval-shaped tumor is considered.

Accordingly, Fig. 5 shows the 2D visuals of segmented output in all three planes namely Axial, Coronal, and Sagittal taken at the same position. The 1st column is the inputs whereas the 2nd, and 3rd column shows the segmented output and contours overlaid on the input images which are highlighted in red color. The outcomes in columns 2 and 3 represent the exactness of BEFVBTS in capturing the tumor boundaries owing to the adopted Bezier that captures the acute shape variations bounding the tumor. Further, to record the robustness of the framework, the quantitative analysis on Duke- Breast-Cancer-MRI was performed and the results are tabulated in Table 1.

In Table 1, the upper arrow (↑) denotes that the metrics with higher values are better, and the lower arrow (↓) denotes that the metrics with lower values are better for the model. All the grades demonstrated consistent results as the framework is capable of offering a fine distinction between the voxels occupying the VOI and non-VOI. The key quality of the energy-tuned functionals based on multivariate Hessian is the major modeling benefit offered by BEFVBTS.

B. SEGMENTATION ON QIN BREAST DCE-MRI

A sample DCE-MRI with a multifocal tumor segmented using BEFVBTS is shown in Fig. 6. The figure depicts the 3D visuals of the segmented output. Upon observing

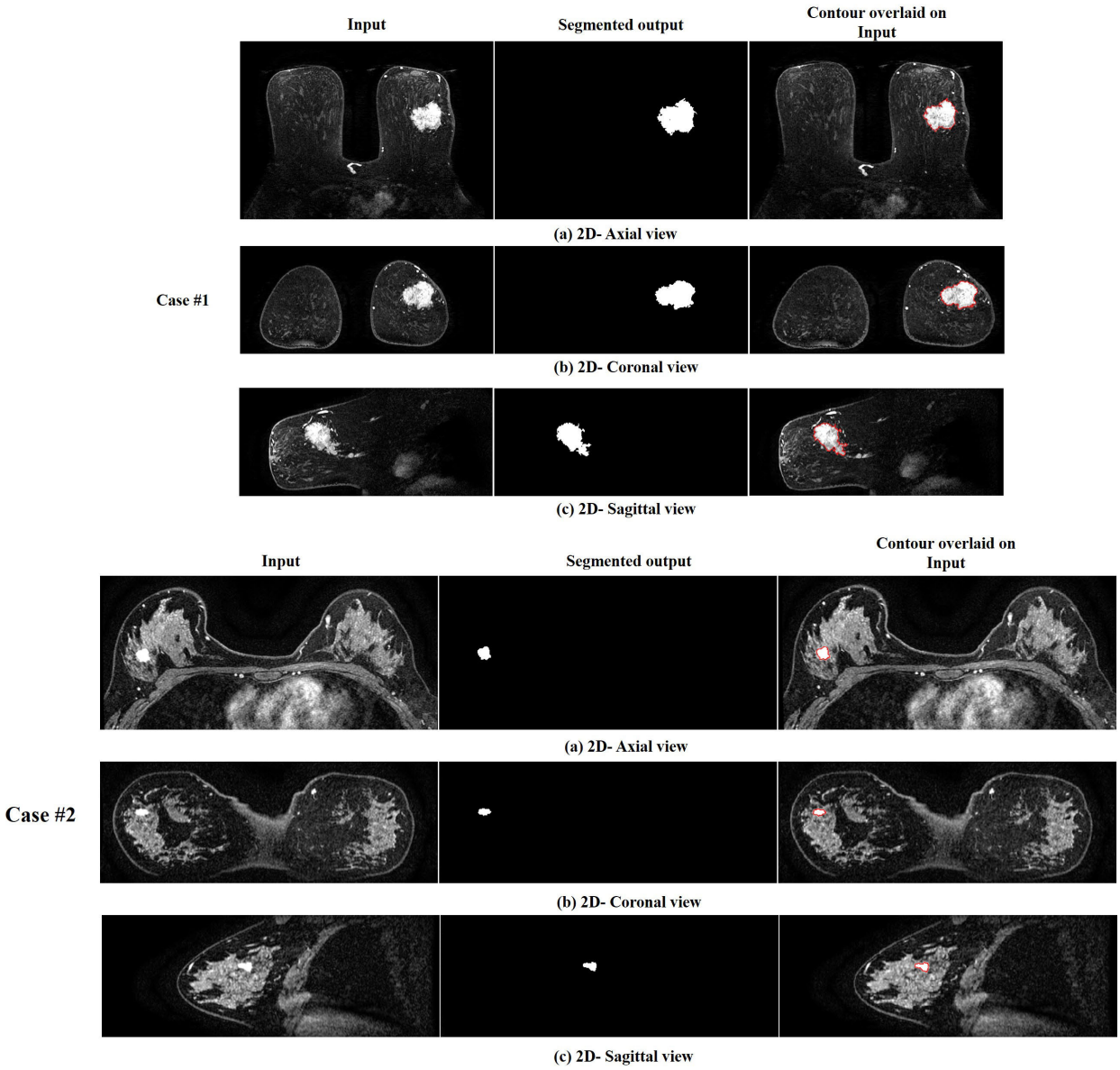

FIGURE 5. Visuals of 2D DCE-MRI depicting segmentation on three planes (Axial, Coronal, Sagittal) using the BEFVBTS framework (Case #1 and Case #2). Column 1 (Original Input), Column 2 (segmented Output), Column 3(Contour overlaid on Input).

Fig. 6 it is evident that the BEFVBTS is reliable in segmenting heterogeneous tumors at ease without any additional computations. For analysis, the post-contrast images were chosen and the ROC metrics were compared with Deep Learning models presented in [22]. Table 2 demonstrates the relative analysis of the proposed framework with its peers. Table 2 outlines the potency of BEFVBTS in the accurate segmentation and the result shows percentage improvement of 8, 22, 8.7, 4, 0.120, and 68.17 in Dice, Jaccard, Precision, Sensitivity, Specificity, and HD respectively. Despite the complex nature of DCE-MRI images consisting of multiple lesions, the framework delivers more consistently than the black-box peers. In addition, the framework has eliminated interpretability by incorporating regularization in convex terms.

C. SEGMENTATION ON TCGA-BRCA

The TCGA-BRCA investigations aim to evaluate only the primary lesions under histopathology conditions using radiomics where the secondary lesions are not involved. These incomplete annotations drag the dice values upon segmentation, affecting overall precision. Therefore, the author [24] complements the annotations as multicentric or multifocal by the expert radiologist including all secondary lesions along with primary. In addition, the registration process is optional since there are no significant differences

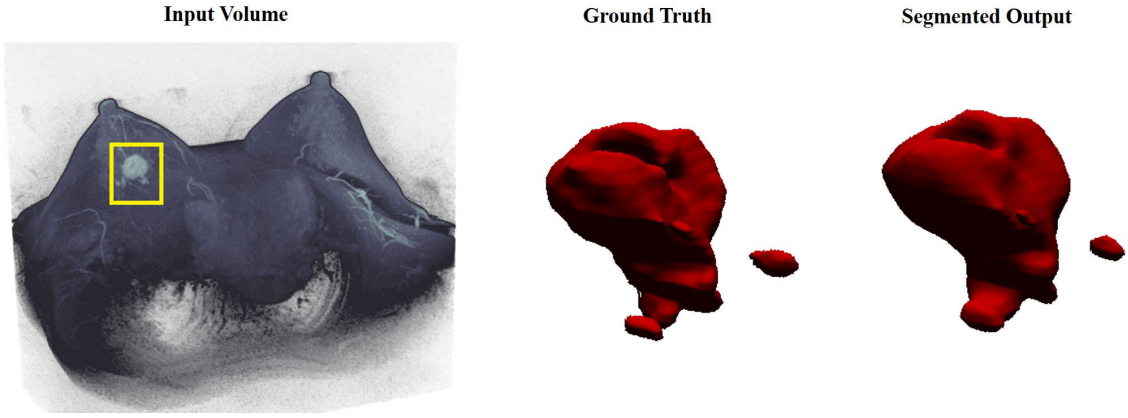

FIGURE 6. 3D Visualization of the tumor volume segmented on a sample QIN breast DCE-MRI dataset with Dice = 0.90 and HD95 = 3.70.

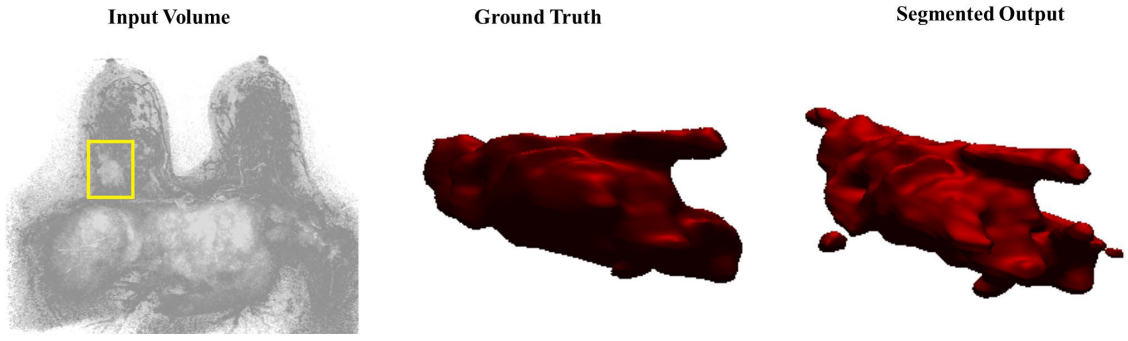

FIGURE 7. 3D Visualization of the tumor (primary) volume segmented on a sample TCGA-BRCA dataset with Dice = 0.92 and HD95 = 3.53 (patient ID -A28Q).

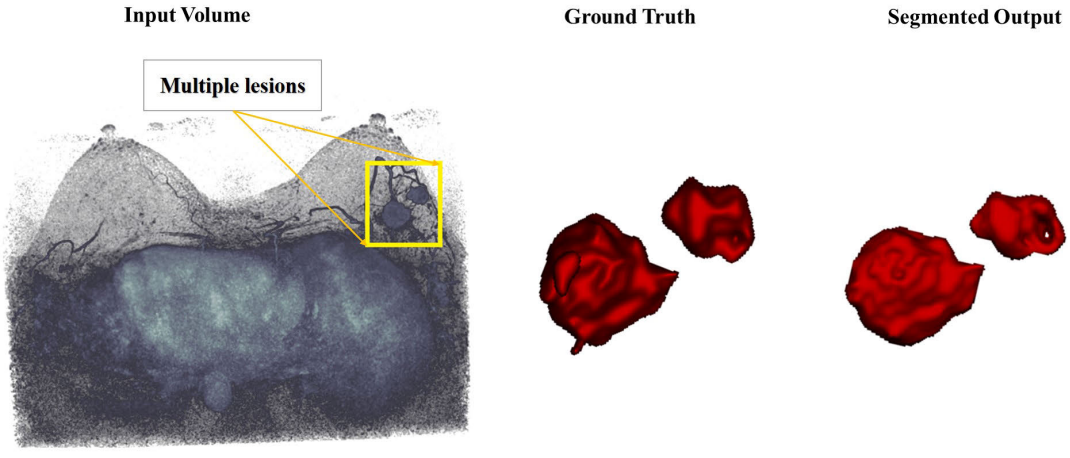

FIGURE 8. 3D Visualization of the tumor (along with secondary) volume segmented on a sample TCGA-BRCA dataset with Dice = 0.87 and HD95 = 3.509 (patient ID -A0DG).

between pre-and post-contrast images. Accordingly, a sample DCE-MRI showing complex structured volume is shown in Fig 7.

Fig 7 & 8 are the 3D visuals of patients A28Q and A0DG depicting multicentric irregularly shaped lesions segmented using BEFVBTS. In general, this dataset seems to be intricate and challenging hence used for BEFVBTS generalization. In addition, a quantitative analysis was performed with the ROC metric including both primary and secondary lesions, and depicted in Table 3.

The dice values reported in Table 3 show that the model is adaptive in segmenting both the primary and secondary lesions with less computation. Also, the overall result depicts that the introduced model efficiently performs volumetric segmentation irrespective of the complexities encountered across the different datasets.

V. COMPUTATIONAL COMPLEXITY

The implementation of the presented segmentation model is studied along the time and space complexities wherein time complexity refers to the total number of elementary operations involved in accomplishing the desired segmentation whilst the space complexity is concerned with the space incurred. To begin with, the overall time complexity in processing the volume size of $m \times n \times$ o is outlined in Eq. (29).

$$Total\ Time = \sum_{i=1}^{N} T_i \approx T_{\max} \tag{29}$$

where T_i is the time complexity of i^{th} module, N is the total number of modules, and $T_{\max}$ is the maximum time taken by the module. The segmentation model initially decomposes the image into three energy constituents by operating on the image volume of dimensions $m \times n \times$ o. Herein $m \times n$ corresponds to the image dimensions with o representing the slice number in the 3D stack. Therefore, the complexity involved in attaining the three diverse energy components is $O(3tmno)$, with t representing the incurred iterations. Likewise, the optimization process initially invokes L2 regularization that demands $O(\log(tmno))$ operations. Later, the hessian of the thresholding matrix is determined to freeze the gradient variations and requires $O((tmno)^2)$ followed by the identification of optimal step size which requires $O((tmno))$ to update the optimized Hessian demanding $O((tmno))$ operations yielding the optimization threshold. The ensuing threshold is then processed by CCA followed by binarization that individually requires $O((mno))$ processing times. The total time complexity of these modules is given in Eq. (30).

$$\begin{aligned} Total\ Time &= O((3tmno)) + O(\log(tmno)) \\ &\quad + O((tmno)^2) + O((tmno)) + O((tmno)) \\ &\quad + O((mno)) + O((mno)) \\ &\approx O((tmno)^2) \end{aligned} \tag{30}$$

The third module has the highest complexity when compared to other modules, hence, the total time complexity is approximate $O((tmno)^2)$. Similarly, space complexity is defined as the amount of memory space utilized by considering the properties of the inputs to solve computational problems. Therefore, the space complexity of the BEFVBTS is $O(mno)$ which considers the input volume size.

VI. CONCLUSION

This work presents an automatic volumetric breast tumor segmentation model engaging variational minimax optimization. The major contribution of this work is the formulation of three energy functionals representing data and regularization terms. The energy minimization process involves finding the optimum heterogeneous volume to interact with the input volume at a high gradient point and updating at each iteration. The updated heterogeneous volume is then binarized and subjected to CCA for residual removal. Further, the adoption Quadratic Bezier curve equation aids in obtaining a non-linear convex combination of the edge-sensitive energy functionals. The self-analysis on the Duke- Breast-Cancer-MRI dataset was conducted to investigate the reliability and consistency of the proposed model. The relative analysis of QIN breast DCE-MRI and TCGA-BRCA datasets shows percentage improvement of 8, 22, 8.7, 4, 0.120, and 68.17 in Dice, Jaccard, Precision, Sensitivity, Specificity, and HD respectively over recent competitors. Also, the complexity analysis reveals the simplicity of the BEFVBTS wherein its counterpart requires more training resources for volumetric segmentation. Hence, the proposed framework for segmenting 3D tumors would assist clinicians in diagnosis and treatment planning. However, the highly energy-centric nature of the introduced segmentation model neglects subtle intensity variations thereby demanding acute optimization along with localization and requires extensive investigation. This limits its extension to other image modalities. Also, local refinement of intensity variations with global characteristics is another setback that requires detailed study when dealing with other modalities and remains an addressable concern.

APPENDIX A

The formulated energy functionals for fixed β, referred to as β^* are shown in Eq. (A.1).

$$\begin{aligned} E(H;\beta) = &\frac{(1-\beta)^2}{3} \iiint (H(x,y,z) - I(x,y,z))^2 dxdydz \\ &+ \frac{2\beta(1-\beta)}{3} \iiint \left(H(x,y,z)^* I(x,y,z)\right)^2 dxdydz \\ &+ \frac{\beta^2}{3} \iiint |\nabla H(x,y,z)|^2 dxdydz \end{aligned} \tag{A.1}$$

The Euler's Equation is given by,

$$E_f = E_H - E_{H_x} - E_{H_y} - E_{H_z} \tag{A.2}$$

where,

$$\begin{aligned} E_{H_x} &= \frac{\partial E}{\partial H_x} = \frac{1}{3}(\beta^*)^2 H_{xx} \\ E_{H_r} &= \frac{\partial E}{\partial H_y} = \frac{1}{3}\left(\beta^*\right)^2 H_{yy} \\ E_{H_z} &= \frac{\partial E}{\partial H_z} = \frac{1}{3}\left(\beta^*\right)^2 H_{zz} \end{aligned}$$

and

$$E_H = \frac{\partial E}{\partial H} = \frac{2}{3}\left(1-\beta^*\right)^2(H-I) + \frac{4}{3}\left(\beta^* - \left(\beta^*\right)^2\right)(I^*H)$$
$$E_f = \frac{2}{3}\left(1-\beta^*\right)^2(H-I) + \frac{4}{3}\left(\beta^* - \left(\beta^*\right)^2\right)(I^*H) - \frac{1}{3}\left(\beta^*\right)^2\left[H_{xx}+H_{yy}+H_z\right]$$

Gradient descent algorithm

$$\frac{\partial H(x,y,z)}{\partial t} = -E_f = -\frac{2}{3}\left(1-\beta^*\right)^2(H-I) - \frac{4}{3}\left(\beta^* - \left(\beta^*\right)^2\right)(I^*H) + \frac{1}{3}\left(\beta^*\right)^2\left(\nabla^2 H\right) \tag{A.3}$$

APPENDIX B

$$E\left(H^{(k)}+\tau^{(k)}\delta H^{(k)}\right) = E_1+E_2+E_3 (B.1)$$
$$E_1 = \frac{1}{3}\left(1-\beta^{(k)}\right)^2\sum\left(H^{(k)}+\tau^{(k)}\delta H^{(k)}-I\right)^2 = \frac{1}{3}\left(1-\beta^{(k)}\right)^2\sum\left(H^{(k)}-I\right)^2 + \frac{\left(\tau^{(k)}\right)^2}{3}\left(1-\beta^{(k)}\right)^2\sum\left(\delta H^{(k)}\right)^2 + \frac{2\tau^{(k)}}{3}\left(1-\beta^{(k)}\right)^2\sum\left(H^{(k)}-I\right)\delta H^{(k)}$$
$$E_2 = \frac{2}{3}[\beta^{(k)}-(\beta^{(k)})^2]\sum\left[I.(H^{(k)}+\tau^{(k)}\delta H^{(k)})\right]^2 = \frac{2}{3}[\alpha^{(k)}-(\beta^{(k)})^2]\sum(I*H^{(k)})^2 + \frac{2(\tau^{(k)})^2}{3}[\beta^{(k)}-(\beta^{(k)})^2]\sum(I*\delta H^{(k)})^2 + \frac{4(\tau^{(k)})}{3}[\beta^{(k)}-(\beta^{(k)})^2]\sum(I^2*H^{(k)}\delta H^{(k)})$$
$$E_3 = \frac{1}{3}(\beta^{(k)})^2\sum\left\|\nabla(H^{(k)}+\tau^{(k)}\delta H^{(k)})\right\|^2 = \frac{1}{3}(\beta^{(k)})^2\sum\left\|\nabla H^{(k)}\right\|^2 + \frac{(\tau^{(k)})^2}{3}(\beta^{(k)})^2\sum\left\|\nabla\delta H^{(k)}\right\|^2 + \frac{2\tau^{(k)}}{3}(\beta^{(k)})^2\sum\nabla H^{(k)}.\nabla(\delta H^{(k)}) \tag{B.1}$$

Also

$$E(H^{(k)}+\tau^{(k)}\delta H^{(k)}) = e_1+\tau^{(k)}e_2+(\tau^{(k)})^2e_3$$

where

$$e_1 = \frac{1}{3}(1-\beta^{(k)})^2\sum(H^{(k)}-I)^2 + \frac{2}{3}\beta^{(k)}(1-\beta^{(k)})\sum(I*H^{(k)})^2 + \frac{1}{3}(\beta^{(k)})^2\sum\left\|\nabla H^{(k)}\right\|^2$$
$$e_2 = \frac{2}{3}(1-\beta^{(k)})^2\sum(H^{(k)}-I)\delta H^{(k)} + \frac{4}{3}\beta^{(k)}(1-\beta^{(k)})\sum(I^2*H^{(k)}\delta H^{(k)}) + \frac{2}{3}(\beta^{(k)})^2\sum\nabla H^{(k)}.\nabla(\delta H^{(k)})$$
$$e_3 = \frac{1}{3}(1-\beta^{(k)})^2\sum(\delta H^{(k)})^2 + \frac{2}{3}\beta^{(k)}(1-\beta^{(k)})\sum(I*\delta H^{(k)})^2 + \frac{1}{3}(\beta^{(k)})^2\sum\left\|\nabla\delta H^{(k)}\right\|^2$$

The optimal step size is given by,

$$\tau^{(k)} = -\frac{e_2}{2e_3} \tag{B.2}$$

ACKNOWLEDGMENT

The authors acknowledge the remarkable support from Dr. Anandh KR, Department of Radiology, Cincinnati Children's Hospital Medical Center, Cincinnati, OH, USA, for qualitative and quantitative evaluation of the developed segmentation model.

REFERENCES

[1] V. F. Grabinski and O. W. Brawley, "Disparities in breast cancer," *Obstetrics Gynecol. Clinics*, vol. 49, no. 1, pp. 149–165, 2022.
[2] D. Trapani, O. Ginsburg, T. Fadelu, N. U. Lin, M. Hassett, A. M. Ilbawi, B. O. Anderson, and G. Curigliano, "Global challenges and policy solutions in breast cancer control," *Cancer Treatment Rev.*, vol. 104, Mar. 2022, Art. no. 102339.
[3] R. L. Siegel, K. D. Miller, H. E. Fuchs, and A. Jemal, "Cancer statistics, 2022," *CA, A Cancer J. Clinicians*, vol. 72, no. 1, pp. 1–28, 2022.
[4] H. Hussein, E. Abbas, S. Keshavarzi, R. Fazelzad, K. Bukhanov, S. Kulkarni, F. Au, S. Ghai, A. Alabousi, and V. Freitas, "Supplemental breast cancer screening in women with dense breasts and negative mammography: A systematic review and meta-analysis," *Radiology*, vol. 306, no. 3, Mar. 2023, Art. no. e221785.
[5] Y. Fang and Y. Zhou, "Diagnosis of breast cancer lesion using ultrasound images, elastography, and ki-67 protein cell proliferation index," *Cellular Mol. Biol.*, vol. 69, no. 4, pp. 16–23, Apr. 2023.
[6] T. Trongtirakul, S. Agaian, and A. Oulefki, "Automated tumor segmentation in thermographic breast images," *Math. Biosci. Eng.*, vol. 20, no. 9, pp. 16786–16806, 2023.
[7] T. Trongtirakul, A. Oulefki, S. Agaian, and W. Chiracharit, "Enhancement and segmentation of breast thermograms," *Proc. SPIE*, vol. 11399, pp. 96–107, Apr. 2020.
[8] D. Wekking, M. Porcu, P. De Silva, L. Saba, M. Scartozzi, and C. Solinas, "Breast MRI: Clinical indications, recommendations, and future applications in breast cancer diagnosis," *Current Oncol. Rep.*, vol. 25, no. 4, pp. 257–267, Apr. 2023.
[9] M. Zhang, B. Mesurolle, M. Theriault, S. Meterissian, and E. A. Morris, "Imaging of breast cancer–beyond the basics," *Current Problems Cancer*, vol. 47, no. 2, Apr. 2023, Art. no. 100967.
[10] M. Kataoka, "Ultrafast DCE-MRI as a new tool for treatment response prediction in neoadjuvant chemotherapy of breast cancer," *Diagnostic Interventional Imag.*, vol. 104, no. 12, pp. 565–566, 2023, doi: 10.1016/j.diii.2023.08.005.

[11] D. Udayakumar, A. J. Madhuranthakam, and B. E. Dogan, "Magnetic resonance perfusion imaging for breast cancer," *Magn. Reson. Imag. Clinics North Amer.*, vol. 32, no. 1, pp. 135–150, Feb. 2024.
[12] Y. Liu, L. Ren, X. Cao, and Y. Tong, "Breast tumors recognition based on edge feature extraction using support vector machine," *Biomed. Signal Process. Control*, vol. 58, Apr. 2020, Art. no. 101825.
[13] B. Mughal, N. Muhammad, and M. Sharif, "Adaptive hysteresis thresholding segmentation technique for localizing the breast masses in the curve stitching domain," *Int. J. Med. Informat.*, vol. 126, pp. 26–34, Jun. 2019.
[14] S.-Y. Wan and W. E. Higgins, "Symmetric region growing," *IEEE Trans. Image Process.*, vol. 12, no. 9, pp. 1007–1015, Sep. 2003.
[15] Y. Cui, Y. Tan, B. Zhao, L. Liberman, R. Parbhu, J. Kaplan, M. Theodoulou, C. Hudis, and L. H. Schwartz, "Malignant lesion segmentation in contrast-enhanced breast MR images based on the marker-controlled watershed," *Med. Phys.*, vol. 36, no. 10, pp. 4359–4369, Oct. 2009.
[16] M. Taheri, G. Hamer, S. H. Son, and S. Y. Shin, "Automated single and multi-breast tumor segmentation using improved watershed technique in 2D MRI images," in *Proc. Int. Conf. Res. Adapt. Convergent Syst.*, Oct. 2016, pp. 61–66.
[17] S. Krinidis and V. Chatzis, "Fuzzy energy-based active contours," *IEEE Trans. Image Process.*, vol. 18, no. 12, pp. 2747–2755, Dec. 2009.
[18] W. Chen, M. L. Giger, and U. Bick, "A fuzzy c-means (FCM)-based approach for computerized segmentation of breast lesions in dynamic contrast-enhanced MR images1," *Academic Radiol.*, vol. 13, no. 1, pp. 63–72, Jan. 2006.
[19] S. C. Agner, J. Xu, and A. Madabhushi, "Spectral embedding based active contour (SEAC) for lesion segmentation on breast dynamic contrast enhanced magnetic resonance imaging," *Med. Phys.*, vol. 40, no. 3, Mar. 2013, Art. no. 032305.
[20] K.-S. Chuang, H.-L. Tzeng, S. Chen, J. Wu, and T.-J. Chen, "Fuzzy c-means clustering with spatial information for image segmentation," *Comput. Med. Imag. Graph.*, vol. 30, pp. 9–15, Jan. 2006.
[21] C. Militello, L. Rundo, M. Dimarco, A. Orlando, V. Conti, R. Woitek, I. D'Angelo, T. V. Bartolotta, and G. Russo, "Semi-automated and interactive segmentation of contrast-enhancing masses on breast DCE-MRI using spatial fuzzy clustering," *Biomed. Signal Process. Control*, vol. 71, Jan. 2022, Art. no. 103113.
[22] J. Ru, B. Lu, B. Chen, J. Shi, G. Chen, M. Wang, Z. Pan, Y. Lin, Z. Gao, J. Zhou, X. Liu, and C. Zhang, "Attention guided neural ODE network for breast tumor segmentation in medical images," *Comput. Biol. Med.*, vol. 159, Jun. 2023, Art. no. 106884.
[23] G. E. Park, S. H. Kim, Y. Nam, J. Kang, M. Park, and B. J. Kang, "3D breast cancer segmentation in DCE-MRI using deep learning with weak annotation," *J. Magn. Reson. Imag.*, vol. 59, no. 6, pp. 2252–2262, 2024, doi: 10.1002/jmri.28960.
[24] R. Khaled, J. Vidal, J. C. Vilanova, and R. Martí, "A U-Net ensemble for breast lesion segmentation in DCE MRI," *Comput. Biol. Med.*, vol. 140, Jan. 2022, Art. no. 105093.
[25] M. Rahimpour, M.-J. Saint Martin, F. Frouin, P. Akl, F. Orlhac, M. Koole, and C. Malhaire, "Visual ensemble selection of deep convolutional neural networks for 3D segmentation of breast tumors on dynamic contrast enhanced MRI," *Eur. Radiol.*, vol. 33, no. 2, pp. 959–969, Sep. 2022.
[26] M. Qiao, S. Suo, F. Cheng, J. Hua, D. Xue, Y. Guo, J. Xu, and Y. Wang, "Three-dimensional breast tumor segmentation on DCE-MRI with a multilabel attention-guided joint-phase-learning network," *Computerized Med. Imag. Graph.*, vol. 90, Jun. 2021, Art. no. 101909.
[27] J. Zhang, A. Saha, Z. Zhu, and M. A. Mazurowski, "Hierarchical convolutional neural networks for segmentation of breast tumors in MRI with application to radiogenomics," *IEEE Trans. Med. Imag.*, vol. 38, no. 2, pp. 435–447, Feb. 2019.
[28] H. Wang, J. Cao, J. Feng, Y. Xie, D. Yang, and B. Chen, "Mixed 2D and 3D convolutional network with multi-scale context for lesion segmentation in breast DCE-MRI," *Biomed. Signal Process. Control*, vol. 68, Jul. 2021, Art. no. 102607.
[29] X. Hu, L. Chu, J. Pei, W. Liu, and J. Bian, "Model complexity of deep learning: A survey," *Knowl. Inf. Syst.*, vol. 63, no. 10, pp. 2585–2619, Oct. 2021.
[30] F.-L. Fan, J. Xiong, M. Li, and G. Wang, "On interpretability of artificial neural networks: A survey," *IEEE Trans. Radiat. Plasma Med. Sci.*, vol. 5, no. 6, pp. 741–760, Nov. 2021.
[31] H. Chen, Y. Deng, B. Li, Z. Li, H. Chen, B. Jing, and C. Li, "BézierSeg: Parametric shape representation for fast object segmentation in medical images," *Life*, vol. 13, no. 3, p. 743, Mar. 2023.
[32] C. Madhu and M. S. Sudhakar, "Adaptive Bezier curve-based membership function formulation scheme for interpretable edge detection," *Appl. Soft Comput.*, vol. 133, Jan. 2023, Art. no. 109968.
[33] O. P. Agrawal, "Formulation of Euler–Lagrange equations for fractional variational problems," *J. Math. Anal. Appl.*, vol. 272, no. 1, pp. 368–379, Aug. 2002.
[34] F. H. Clarke, "The Euler–Lagrange differential inclusion," *J. Differ. Equ.*, vol. 19, no. 1, pp. 80–90, Sep. 1975.
[35] J. L. Troutman, *Variational Calculus With Elementary Convexity*. Berlin, Germany: Springer, 2012.
[36] P. E. Gill, W. Murray, and M. H. Wright, *Practical Optimization*. Philadelphia, PA, USA: SIAM, 2019.
[37] R. C. Gonzalez, *Digital Image Processing*. London, U.K.: Pearson, 2009.
[38] R. D. Yapa and H. Koichi, "A connected component labeling algorithm for grayscale images and application of the algorithm on mammograms," in *Proc. ACM Symp. Appl. Comput.*, Mar. 2007, pp. 146–152.
[39] F. Chang, C.-J. Chen, and C.-J. Lu, "A linear-time component-labeling algorithm using contour tracing technique," *Comput. Vis. Image Understand.*, vol. 93, no. 2, pp. 206–220, Feb. 2004.
[40] K. Clark, B. Vendt, K. Smith, J. Freymann, J. Kirby, P. Koppel, S. Moore, S. Phillips, D. Maffitt, M. Pringle, L. Tarbox, and F. Prior, "The cancer imaging archive (TCIA): Maintaining and operating a public information repository," *J. Digit. Imag.*, vol. 26, no. 6, pp. 1045–1057, Dec. 2013.

PRIYADHARSHINI BABU is currently pursuing the Ph.D. degree in tumor segmentation, analysis, and treatment response in breast cancer. She is a Research Scholar under the supervision of Dr. Mythili Asaithambi who is a Professor with the Sensor and Biomedical Technology Division, School of Electronics Engineering, Vellore Institute of Technology, Vellore, India.

MYTHILI ASAITHAMBI received the Ph.D. degree from Madras Institute of Technology, Anna University. She availed DST-PURSE fellowship during the Ph.D. degree. She is currently a Professor with the Sensor and Biomedical Technology Division, School of Electronics Engineering, Vellore Institute of Technology, Vellore, India. She has published more than 30 papers in journals and conferences. Her current research interest includes medical image processing with machine learning.

SUDHAKAR MOGAPPAIR SURIYAKUMAR is currently an Associate Professor with the School of Electronics Engineering, Vellore Institute of Technology, Vellore, India. He has several years of industrial and research and development experience in tier-1 organizations. He has authored or coauthored a sufficient number of research articles in Science Citation Index journals and also the PI of a research project with Indian Space Research Organisation (ISRO). His research interests include machine learning and its applications, such as computer vision, data mining, image processing, information retrieval, and pattern recognition.